MR imaging and volume localized spectroscopy: Medical and materials applications

N. Chandrakumar

Chemical Physics, Central Leather Research Institute, Adayaru, Madras 600 020, India

The principles of magnetic resonance imaging are introduced. The basis is a resonance experiment where spatial information is built into the frequency, phase or amplitude of processing magnetization by the application of magnetic field gradients or rf gradients. The field of view, resolution and contrast of MR images are defined and the limitations on resolution are discussed. In this context, both NMR and ESR imaging are considered explicitly. The unique possibilities offered by MR image contrast are highlighted. Experimental protocols of Fourier imaging and projection reconstruction imaging are described, in terms of the phase sensitive detection capability of the MR receiver, the trajectory of the reciprocal space vector, procedures for gradient controlled 'slice' selection, and the advantages of echo detection. Gradient and spin echo imaging, as well as chemical shift selective imaging are dealt with and the principles of multiply selective Hadamard excitation discussed, as also some novel alternatives for selective excitation. Pulse sequences for three dimensional imaging as well as four-dimensional spatial-spectral imaging are briefly introduced. Applications from our laboratory are employed to illustrate the various methods. The special requirements of metabolite imaging are spelt out and the development and applications of multiple quantum imaging in our laboratory discussed in some detail. Volume localized spectroscopy is introduced as an alternative spatial-spectral procedure. The basis of single scan volume localization is then dealt with, with reference to a specific three-pulse sequence. The development, implementation and application of two-dimensional volume localized zero quantum spectroscopy for *in vivo* applications is then briefly described. Finally, MR imaging of solids is introduced, and an illustration of stray field imaging from our laboratory is included. The article finally calls attention to the novel approach of magnetic resonance force microscopy as well.

WHEN a cylindrical tube filled with water is placed in a homogeneous magnetic field B_0 – with the long axis of the tube parallel to the direction z of the field – and excited by a burst of resonant radiation, a free induction decay (FID) results following excitation. Upon Fourier transformation, a single sharp signal results, this being the NMR spectrum of the water protons (Figure 1).

If this experiment were repeated under identical conditions, except that a gradient parallel to B_0 were superimposed on the field, eg. by a current passing in a pair of coils in anti-Helmholtz configuration, the resulting FID includes a distribution of resonance frequencies. Its Fourier transform has a top hat profile which corresponds to the profile of the sample tube along z (Figure 2).

By reorienting the direction of the gradient with respect to the tube, a number of such profiles may be obtained, and the image of the tube can then be reconstructed by suitable projection reconstruction or by filtered back projection techniques. This idea was first demonstrated by Lauterbur twenty-two years ago[1]; he went on to obtain the first actual NMR images, which

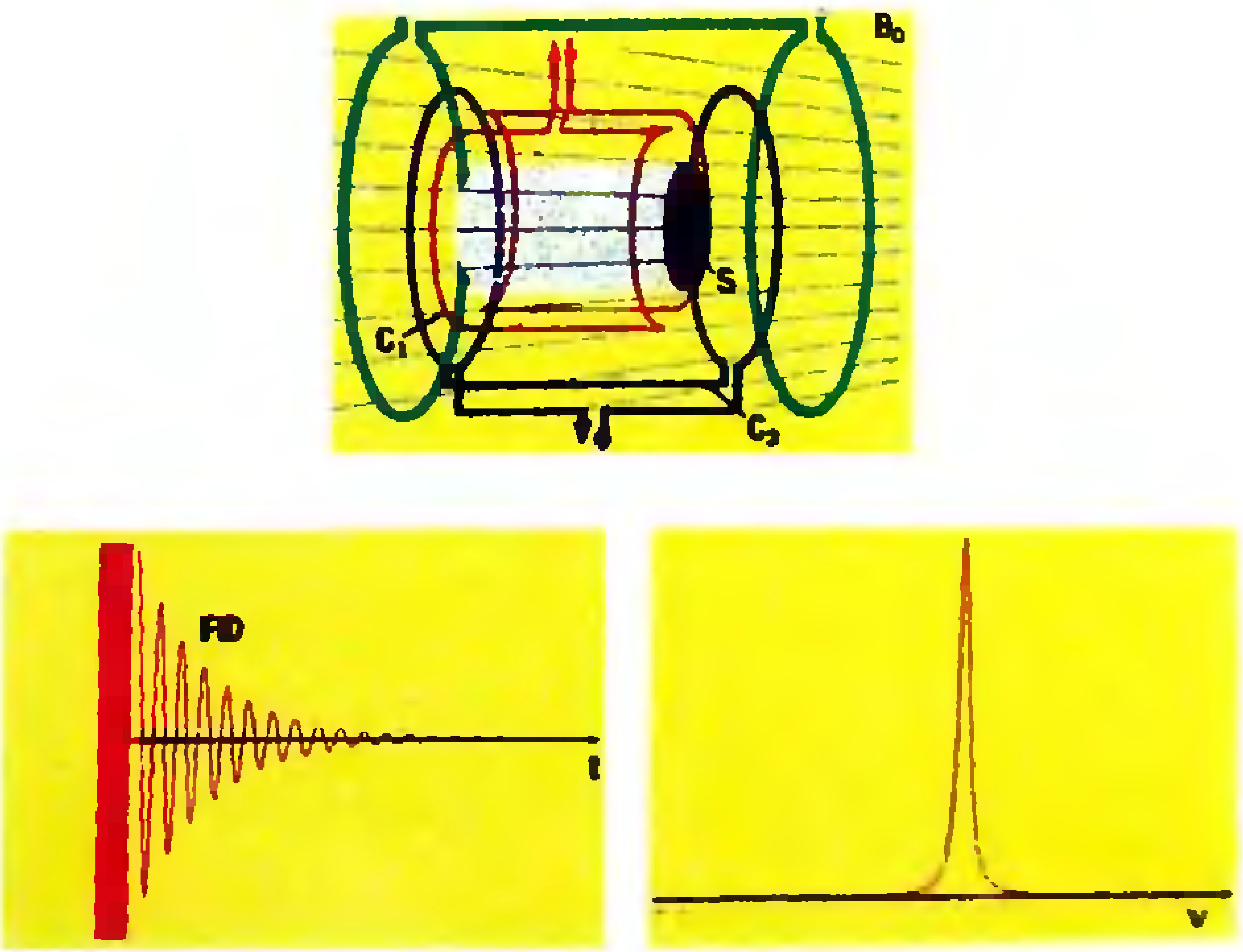

Figure 1. *Top*: Experimental set-up for MR spectroscopy and imaging. The green coil produces the main homogeneous dc magnetic field B_0, the red coil C_1 serves for rf excitation at the resonance frequency, while the dark brown coil C_2 in anti-Helmholtz configuration produces a field gradient when a current is passed through it. The green flux lines in the background illustrate this. *Bottom left*: RF pulse excitation followed by the free induction decay signal from the sample, obtained without any current passing through the coil C_2. The receiver is gated on following the excitation pulse from the transmitter. *Bottom right*: Fourier transform of the FID on the left, leading to the frequency spectrum of the sample.

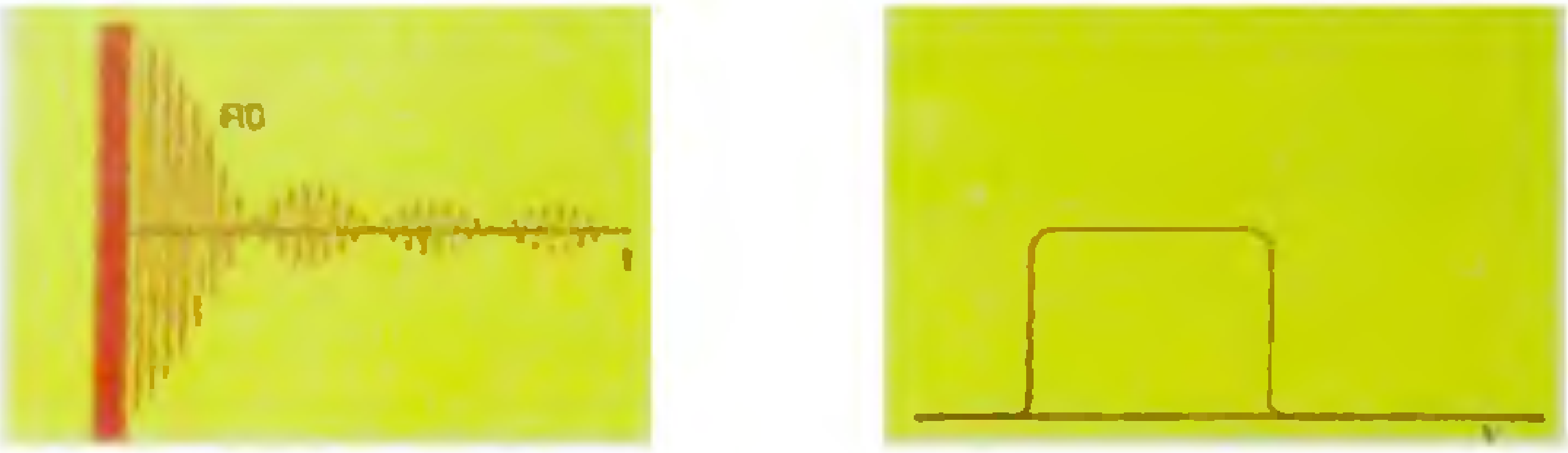

Figure 2. *Left*: RF pulse excitation followed by the free induction decay signal from the sample, obtained in the presence of a gradient generated by passing a current through the gradient coil C_2. Note the complex shape of the FID, corresponding to the presence of a distribution of frequencies. *Right*: Fourier transform of the FID on the left, leading to the frequency spectrum of the sample. With a calibrated gradient strength, the frequency axis may be represented equivalently as a spatial co-ordinate axis. The spectrum now corresponds to the profile of the object along the gradient direction.

were those of a section of the thoracic cavity of a live, anaesthetized mouse. On his grayscale image, the visualization of organs was possible on the basis of the water distribution; in particular, the lungs showed up remarkably clearly. Since then, magnetic resonance imaging has developed into a powerful and much sought after technique for diverse applications. In the meantime, the twin area of electron spin resonance imaging has also developed gradually.

The physical basis of magnetic resonance imaging is, as the name implies, not scattering, but a resonance phenomenon. It may be recalled that in a standard imaging experiment that works by scattering, the image resolution can be no better than the wavelength of the radiation that is scattered. On the one hand, radiation wavelengths that are employed for NMR imaging, for example, are typically in the range of *metres*, being based on radiofrequencies; a scattering experiment relying on such radiation wouldn't be adequate to image an elephant! On the other hand, high resolution MR experiments do not sense spatial co-ordinates at all. In MR imaging, therefore, spatial information of the object to be imaged is *encoded* into frequency, phase or sometimes amplitude information by means of dc or sometimes rf field gradients. MR imaging, therefore, is something of a counter-intuitive experiment, both in terms of standard imaging practice, as well as of standard MR spectroscopy.

The encoding of spatial information by means of field gradients may be readily seen as follows. We begin with the basic definition of the gradient tensor:

$$\bar{\bar{\mathbf{G}}} = \begin{pmatrix} \dfrac{\partial B_x}{\partial x} & \dfrac{\partial B_x}{\partial y} & \dfrac{\partial B_x}{\partial z} \\ \dfrac{\partial B_y}{\partial x} & \dfrac{\partial B_y}{\partial y} & \dfrac{\partial B_y}{\partial z} \\ \dfrac{\partial B_z}{\partial x} & \dfrac{\partial B_z}{\partial y} & \dfrac{\partial B_z}{\partial z} \end{pmatrix} \qquad (1)$$

With the direction of the dc field $\mathbf{B}_0$ defined as z, the field gradient may be expressed as a vector:

$$\vec{\mathbf{G}} = \hat{\mathbf{i}}\left(\frac{\partial B_0}{\partial x}\right)_{y,z} + \hat{\mathbf{j}}\left(\frac{\partial B_0}{\partial y}\right)_{z,x} + \hat{\mathbf{k}}\left(\frac{\partial B_0}{\partial z}\right)_{x,y} \qquad (2)$$

We now have for the Larmor frequency of the spin in the magnetic field:

$$\begin{aligned} \omega &= -\gamma B_0 - \gamma(\vec{\mathbf{G}} \cdot \vec{\mathbf{r}}) \\ &= -\gamma B_0 - \gamma\left[x\left(\frac{\partial B_0}{\partial x}\right)_{y,z} + y\left(\frac{\partial B_0}{\partial y}\right)_{z,x} + z\left(\frac{\partial B_0}{\partial z}\right)_{x,y}\right]. \end{aligned} \qquad (3)$$

This corresponds to a position-dependent frequency shift. By the same token, a position-dependent phase shift may also be defined in terms of the time integral of the frequency:

$$\phi(t) = \int_0^t \omega(t')\mathrm{d}t'. \qquad (4)$$

Measurement of these frequency or phase shifts therefore produces the desired spatial information in the MR spectrum, corresponding to the image that is sought.

The parameters of MR imaging

The original projection reconstruction experiment of Lauterbur is in the spirit of standard X-ray-based imaging methods, relying on acquiring a series of projections at various orientations and employing these to reconstruct the desired image. It was soon realized, however, that the NMR imaging experiment could be performed in quite another fashion, in the manner of multidimensional NMR spectroscopy[2]. This mode of MR image acquisition is Fourier imaging. In short, it is possible to perform Fourier MR imaging – as long as phase memory times of transverse magnetization are considerably longer than gradient switching times – because MR has no phase problem associated with it: unlike the case of X-rays, the MR detector is phase sensitive.

A current popular version of a simple imaging sequence on the basis of this principle is given in Figure 3.

This sequence involves excitation of the transverse magnetization from a slice of the object by means of a shaped, selective rf pulse in the presence of the slice selection gradient G_S. The gradient G_S results in a dispersal of the Larmor frequency along its direction, notionally dividing the object into a number of parallel planes ('slices') perpendicular to this direction. A specific slice of finite thickness is selected for imaging by employing a frequency selective excitation pulse with small, finite bandwidth. Desirable slice profiles do not result with the standard rectangular pulse envelope, but instead demand complex pulse envelope modulation. Following the creation of transverse magnetization from the chosen slice, this magnetization is phase encoded under the influence of a gradient G_P that is orthogonal to G_S; it is then frequency-encoded in the third orthogonal direction employing the gradient G_R during signal acquisition. The experiment is then repeated with the sole variation that the amplitude of the phase encode gradient G_P is systematically incremented from experiment to experiment. This set of experiments generates a two-dimensional dataset, viz. a set of frequency encoded FIDs acquired as a function of variable phase encode gradient amplitude.

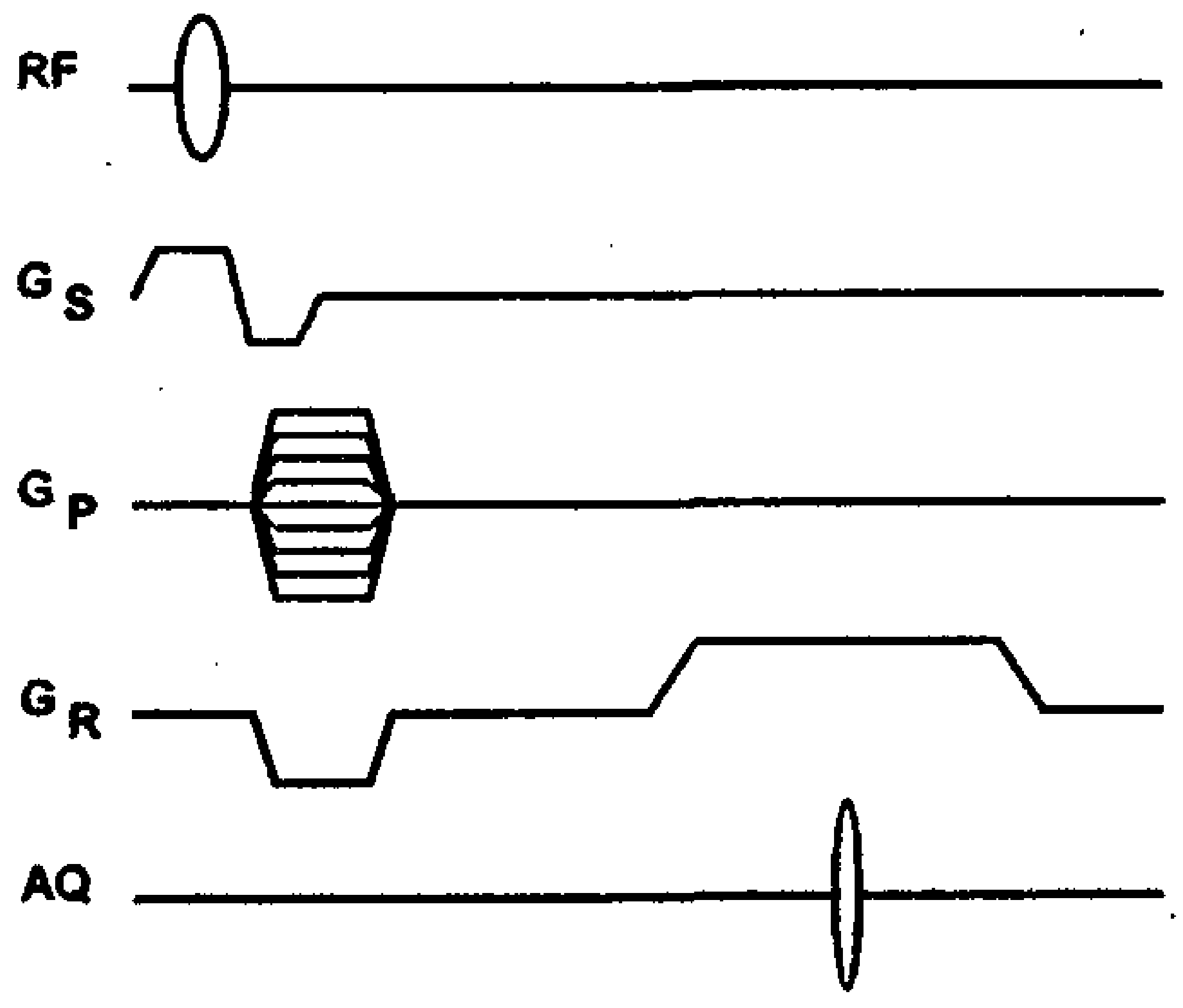

Figure 3. Pulse sequence for two-dimensional Gradient Echo MR imaging of a selected slice of the object. The shaped RF pulse applied in the presence of a slice selection gradient G_S results in transverse magnetization from the chosen slice, which is then phase encoded and subsequently frequency encoded. The sequence is repeated with systematic incrementation of the phase encode gradient amplitude G_P. Note that this strategy to generate the two-dimensional dataset is substantially different from the standard 2D NMR approach of evolution time incrementation; in the imaging sequence, the evolution time is held constant while the degree of phase modulation of the FID is varied by taking recourse to incrementation of the phase encode gradient amplitude. This scheme has clear advantages in terms of constant, minimal T_2 losses for the entire 2D dataset.

Three aspects of the experiment deserve further comment: (i) reversal of G_S immediately after slice selection; (ii) application of a reversed read gradient essentially during this period; (iii) acquisition of an echo signal. The reversal of G_S rephases magnetization that is dephased during excitation by the slice selective pulse. The application of an initial reversed read gradient (known as read balance or read trim gradient) leads to dephasing of the transverse magnetization, which is subsequently rephased under G_R, resulting in a gradient echo in the acquisition window. The preferability of echo acquisition relates to the fact that the signal is acquired after the read gradient has been switched on and allowed to settle, so that it is free from the dephasing influence of eddy currents that arise from gradient switching. Echo acquisition also results in a two-fold sensitivity improvement as compared to the acquisition of an FID, since an echo is essentially two back-to-back FIDs. Finally, the imaginary part of the complex FT of an echo vanishes, which means that the image may be presented in magnitude mode without loss of resolution. The last two aspects are spelt out explicitly below, comparing the complex Fourier transform of an FID with that of an echo:

$$\int_{-\infty}^{\infty} u(t)\exp(-at)\exp(-\mathrm{i}\omega t)\mathrm{d}t$$

$$\equiv \int_{0}^{\infty} \exp(-at)\exp(-\mathrm{i}\omega t)\mathrm{d}t$$

$$= (a+\mathrm{i}\omega)^{-1}$$

$$\equiv \frac{a}{(a^2+\omega^2)} - \mathrm{i}\frac{\omega}{(a^2+\omega^2)} \tag{5}$$

$$\int_{-\infty}^{\infty} \exp(-a|t|)\exp(-\mathrm{i}\omega t)\mathrm{d}t = \frac{2a}{(a^2+\omega^2)}. \tag{6}$$

In the spirit of imaging science, we may define fields of view in MR imaging experiments as follows:

$$(\mathrm{FOV})_R\,(\mathrm{cm}) = \frac{1}{2 * \mathrm{DW} * G_R} = \frac{\text{Spectral width (kHz)}}{\text{Read gradient (kHz cm}^{-1}\text{)}},$$

$$(\mathrm{FOV})_P = \frac{1}{\Delta t_P * G_P} = \frac{1}{t_P * \Delta G_P}. \tag{7}$$

These relations show that the fields-of-view are inversely related to the respective gradient amplitudes or gradient increments, and encode durations or duration increments. DW is the digitizer dwell time, while t_P is the phase encode duration. The aspect ratio x of the Fourier MR image is under the experimenter's control:

$$\Delta G_P = \frac{2x(\mathrm{DW})(G_R)}{t_1}, \tag{8}$$

$$x = \frac{(\mathrm{FOV})_R}{(\mathrm{FOV})_P}. \tag{9}$$

The next question that arises in NMR imaging is that related to the attainable image resolution. Clearly, this depends on the gradient amplitudes employed; however, it also depends on the signal-to-noise ratio per voxel (volume element) of the acquired image. To a degree these two parameters are under the control of the experimenter, the signal-to-noise ratio being a function of the field intensity B_0. With a natural linewidth of ca. 10 Hz, proton imaging with a gradient amplitude of ca. 5 G cm^{-1} leads to image resolutions of ca. 5 μ. However, there is a more fundamental limitation in liquid state imaging, which relates to the rms path lengths under random diffusional processes. Given phase or frequency encode durations of the order of 1 ms and a diffusion coefficient D of the order of 10^{-5} cm^2 s^{-1}, we see that the rms path lengths in question are given by:

$$\overline{x^2} = 2Dt,$$

$$\Rightarrow \sqrt{\overline{x^2}} = (\sqrt{2} \times \sqrt{10^{-5} \times 10^{-3}})\,\mathrm{cm} = 1.414\mu. \tag{10}$$

This is the fundamental limit on the resolution achievable in NMR imaging in the liquid state. This level of resolution is clearly inferior to other methods of microscopy, being at best on par with optical microscopy. In ESR imaging in the pulsed mode, on the other hand, frequency encode/echo readout durations could be of the order of 10 μs, so the diffusion path length amounts to about 140 mμ. The limitation in ESR imaging in the solution state is primarily the gradient strength, since even extremely narrow ESR resonances have linewidths of ca. 70 kHz, which translates to a requirement of gradient strengths of ca. 250 G cm^{-1} to achieve resolutions of ca. 1 μ, given free-electron-like g-factors. Realistic resolutions achievable with the narrowest ESR lines therefore amount to ca. 50 μ with a gradient strength of ca. 5 G cm^{-1}.

MR imaging finds valuable application over a wide range of 'sample' dimensions: from whole-body clinical MRI of humans with an in-plane resolution of ca. 1 mm and slice thickness of a few mm, to microimaging of materials and small biological objects with an in-plane resolution of ca. 5 μ and slice thickness of a few hundred microns[3,4].

The unique power of MR imaging is however, not its resolution, but rather its contrast capability. Indeed, the experimenter has a number of magnetic contrast parameters that can be accessed in NMR imaging: viz. the nuclear isotope, the chemical shift, the nuclear spin density, nuclear magnetic relaxation times (T_1, T_2, etc.), as well as flow and diffusion phenomena. We may mention that occasionally paramagnetic contrast agents (eg. complexes of rare earths) are found useful to induce contrast in clinical applications; moreover, it has been demonstrated in recent years that an endogenous BOLD contrast mechanism (*B*lood *O*xygenation *L*evel-*D*ependent) operates in producing functional MR images that enable visualization of activity[5].

Imaging sequences

As is the case with MR spectroscopy, a number of pulse sequences and experiment protocols are valuable in MR imaging under a variety of conditions. We give below a brief summary of some of the more useful NMR imaging sequences.

The various pulse sequences may be classified into different categories with respect to their scan trajectory in time domain. One may define a reciprocal space vector **k** much as in discussions of diffraction experiments, in spite of the fact that the *physical* phenomenon under discussion here is not diffraction, as explained earlier:

$$\vec{\mathrm{k}}(t) = \gamma \int_0^t \vec{\mathrm{G}}(t')\mathrm{d}t'. \tag{11}$$

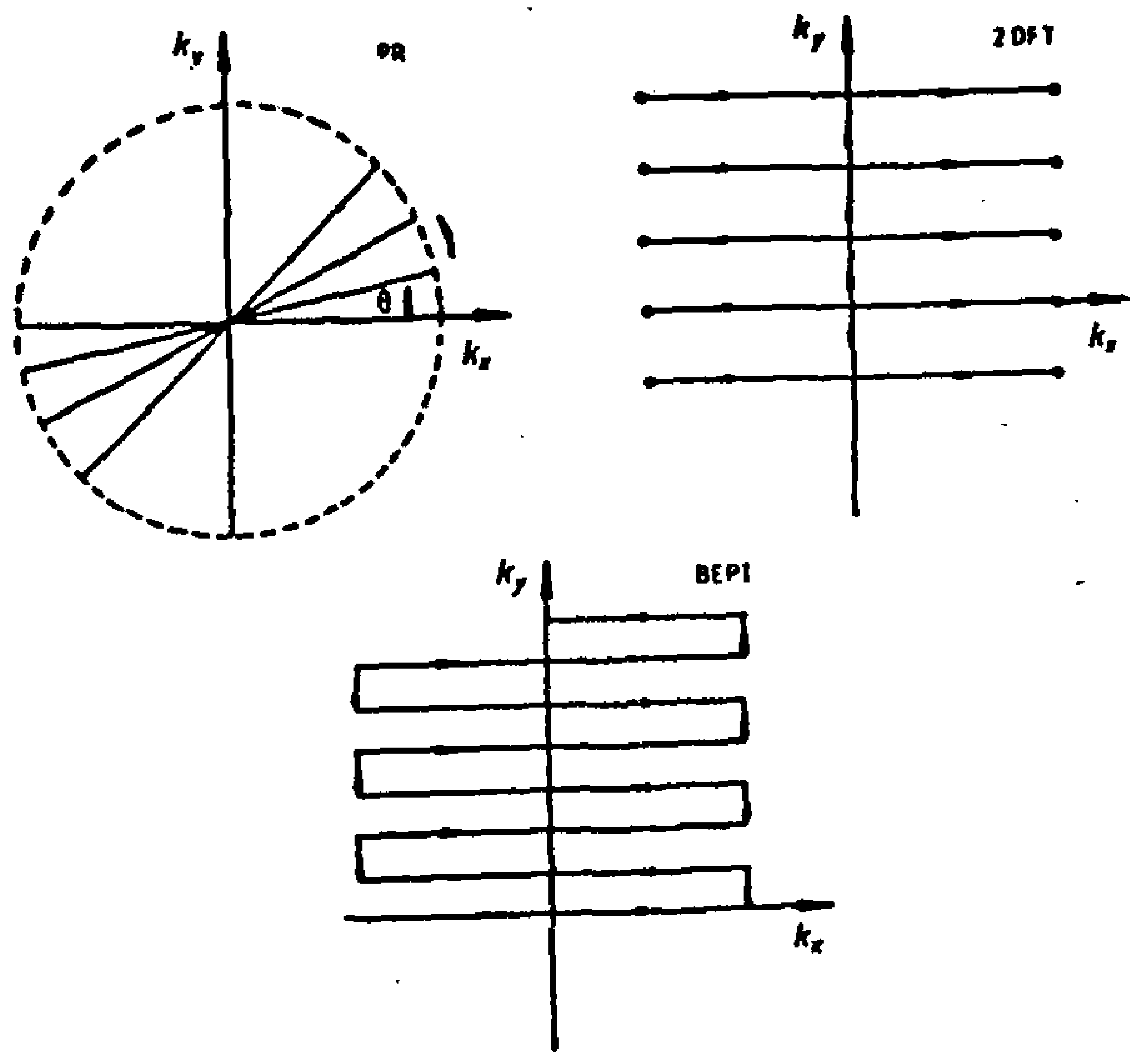

Figure 4. k space trajectories for two-dimensional versions of three imaging sequences, viz. projection reconstruction imaging, Fourier imaging and 'blipped' echo planar imaging.

In particular, **k** space rasters[6] for three categories of MR imaging experiments are noteworthy: projection reconstruction, Fourier imaging and echo planar imaging[7]. The latter is an experiment which involves the formation of a train of gradient echoes by a train of phase-alternated gradient pulses. In this description, projection reconstruction imaging involves radial scans in **k** space, Fourier imaging involves parallel scans in **k** space, while echo planar imaging traverses the entire **k** space in a single pass. These three trajectories are shown in Figure 4.

Other complex trajectories are also possible, especially spiral scans. Echo planar imaging methods are the fastest-known MR imaging methods, although the simple one-pulse gradient echo method of Figure 3 is also extremely fast when employed with low rf pulse flip angles[8], well below 90°. The gradient echo sequence permits short gradient echo times and high repetition rates.

The spin echo imaging sequence is shown in Figure 5. It is characterized by a hard 90° pulse and a slice selective 180° pulse. The echo that is acquired is now not a gradient echo, but rather a spin echo, which is generated by the refocusing 180° rf pulse. The spin echo has certain important characteristics that distinguish it from the gradient echo. Chief among these is the fact that the spin echo refocuses field inhomogeneity effects and chemical shifts while the gradient echo fails to do so, refocusing merely the dephasing under the gradient.

The spin echo times in this sequence may be reduced by arranging to issue the slice refocusing gradient during the phase encode period instead of after the slice selection process. In general, the spin echo imaging sequence is made faster by generating multiple echoes, eg. by a Carr-Purcell train of refocusing pulses[9]. It appears true to say that in general, imaging of 'large' heterogeneous samples on 'small bore' magnets is frought with severe problems in the gradient echo mode, while spin echo experiments succeed handsomely in such applications. An example of a spin echo image of an extruded sample obtained in our laboratory following water ingress is shown in Figure 6. The echo time employed here is 5.5 ms.

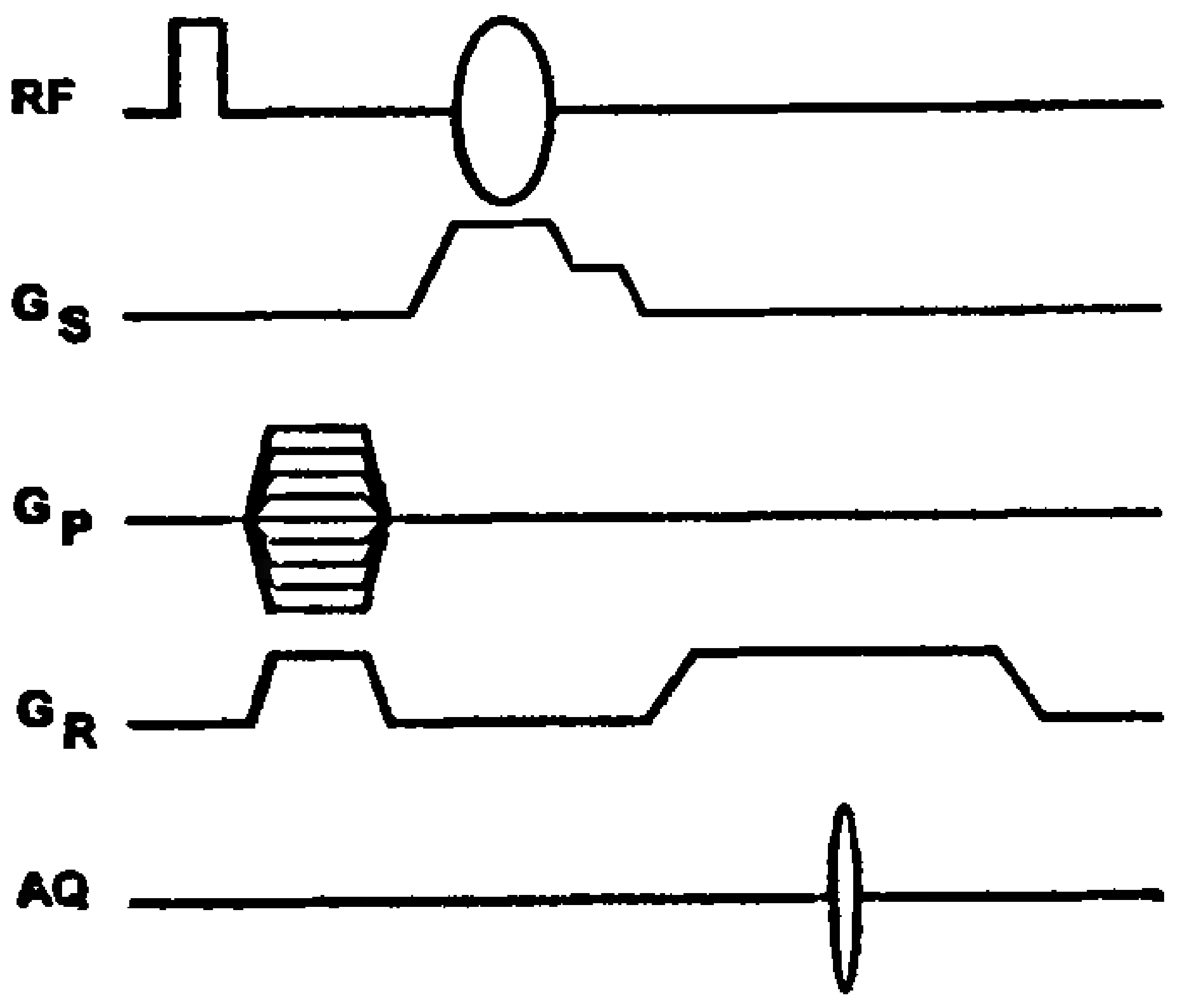

Figure 5. Spin echo MR imaging sequence operated in slice selective 2D mode.

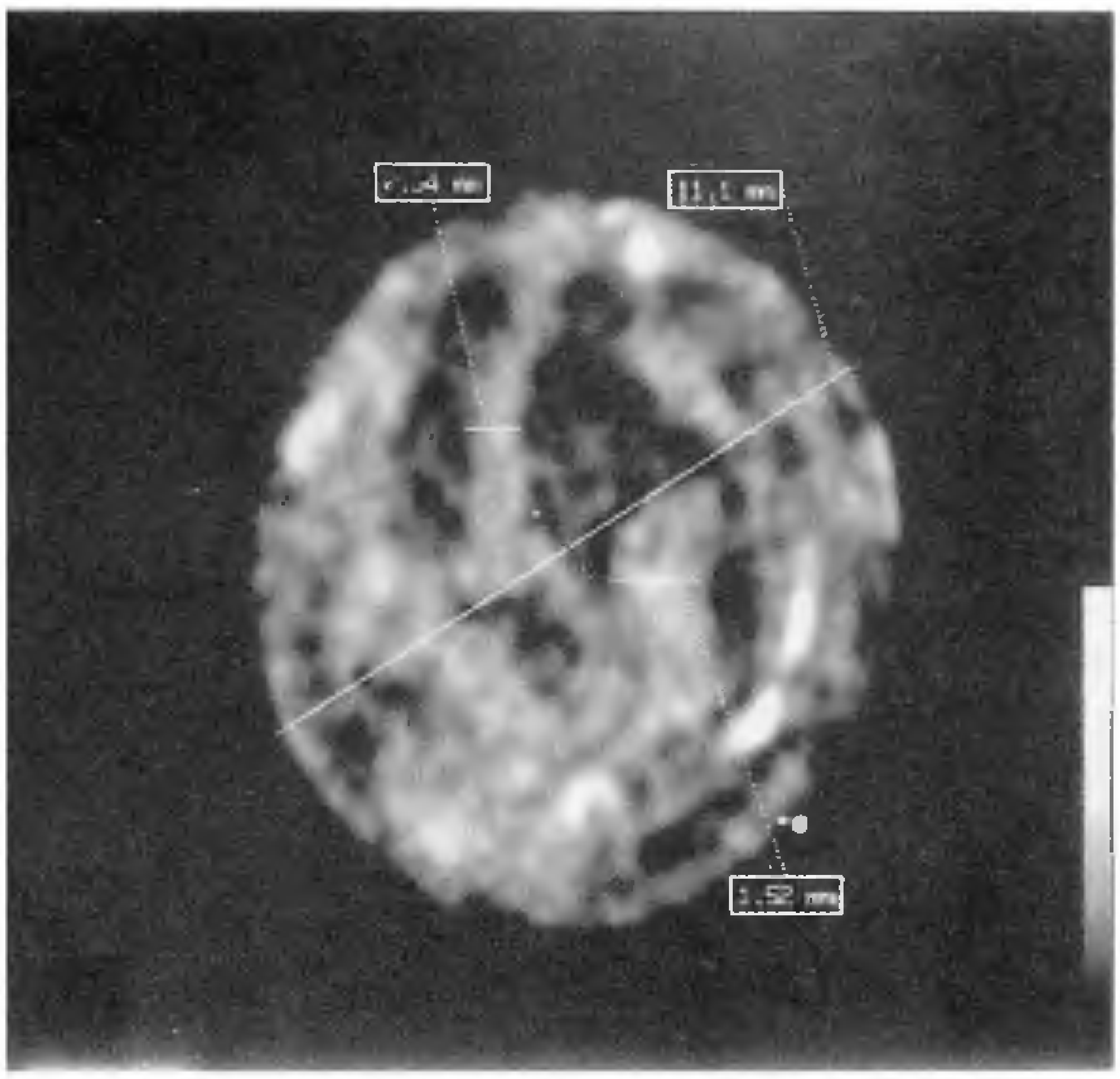

Figure 6. Spin echo image of fluid ingress in an extruded sample; echo time: 5.5 ms.

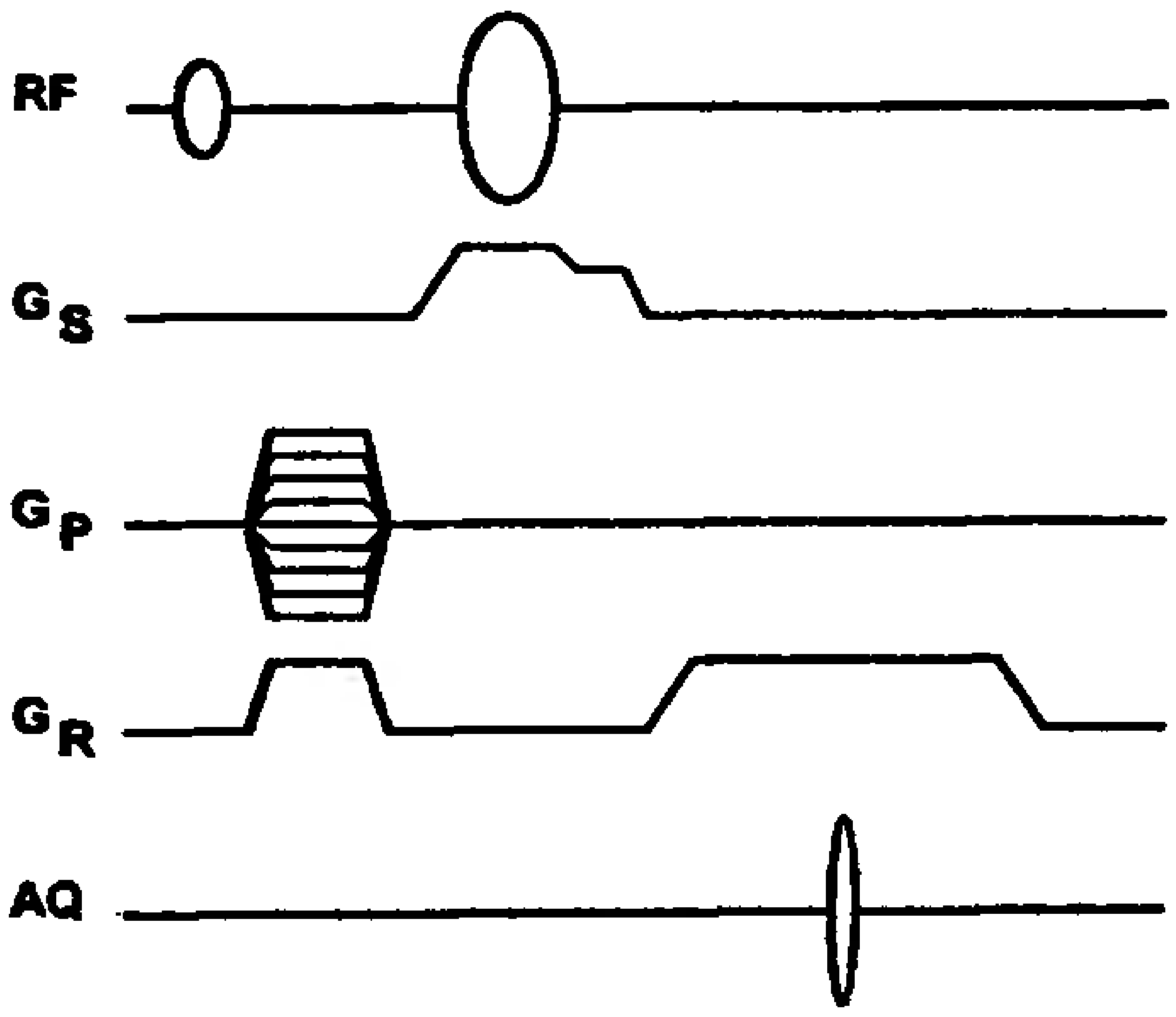

Figure 7. Chemical shift selective spin echo MR imaging sequence, operated in slice-selective 2D mode.

The spin echo sequence may be readily made chemical shift selective by substituting the first hard 90° pulse with a frequency (chemical shift) selective shaped pulse, issued in the absence of a gradient as shown in Figure 7. It is to be noted that shaped pulses are called upon to perform multiple duties in NMR imaging: in the presence of gradients, they are slice selective, while in the absence of gradients they are multiplet selective or transition selective. This parallels the fact that frequency information stands for both spatial co-ordinates, as well as molecular chemical shifts. In the absence of shift selection, image 'artifacts' could arise on imaging molecules with more than one chemical shift or an object with a mixture of molecular components: different chemically-shifted species would give rise to images of the same slice that appear 'offset' in space under conditions of non-selective excitation – except at low fields, where the shift differences fall within the slice thickness.

An early chemical shift selective image of an intact okra obtained in our laboratory is shown in Figure 8. Note especially the water selective and fat selective images.

It is possible to perform the slice-selective experiment in a multi-slice mode – if necessary with interleaving of slices – to generate images of a series of notional slices of the object, thus recovering three-dimensional information. It is also possible to perform multi-slice imaging by a Hadamard technique[10] that relies on multiply-selective excitation to simultaneously excite more than one slice of the object; eg. two, four or eight slices may be simultaneously excited.

$$f_N(t) \sim f(t)\sum_j a_j \exp(\mathrm{i}\omega_j t). \tag{12}$$

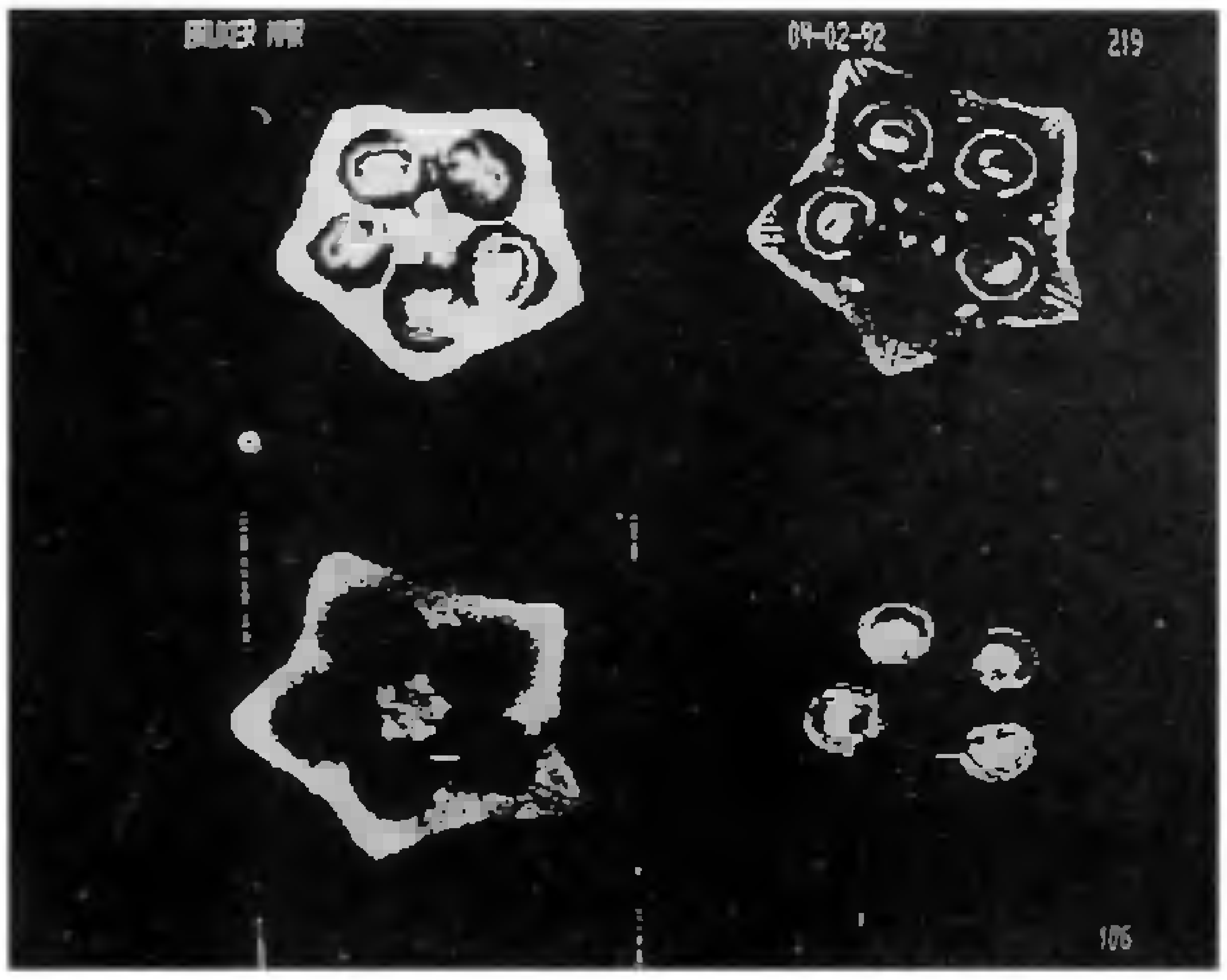

Figure 8. Images of an intact whole-okra. *Top*: Single slice NMR images of two different okra specimens, obtained with two different contrast settings. *Bottom*: Single slice chemical shift selective NMR images of the okra of top right. *Bottom left*: water selective; *Bottom right*: fat selective.

This approach relies on the frequency shift theorem in Fourier transform theory.

$$F(\omega) = \int_{-\infty}^{\infty} f(t)\exp(-\mathrm{i}\omega t)\mathrm{d}t$$

$$\Rightarrow \int_{-\infty}^{\infty} f(t)\exp(\mathrm{i}\omega_0 t)\exp(-\mathrm{i}\omega t)\mathrm{d}t = F(\omega-\omega_0). \tag{13}$$

Upon repeating the excitation, changing the sign of amplitude coefficients a_j at each frequency in turn, in accordance with the rows of a coefficient matrix A, a set of multi-slice profiles may be obtained; on linear combination of the resulting datasets according to the columns of the coefficient matrix A, the images of the individual slices are recovered, with a signal-to-noise improvement per unit measurement time, owing to the multiplex advantage. The Hadamard matrix A has, for example, the following structure for a four-slice excitation–detection sequence:

$$\mathrm{A} = \begin{pmatrix} -1 & 1 & 1 & 1 \\ 1 & -1 & 1 & 1 \\ 1 & 1 & -1 & 1 \\ 1 & 1 & 1 & -1 \end{pmatrix} \tag{14}$$

This strategy works better than might be feared on grounds of the inherent non-linearity of the spin system. Hadamard excitation schemes have been shown[10] to yield high-quality cardiac images; it is now possible to obtain 'MR movies' of the heart over the cardiac cycle.

We have recently established the possibility to perform selective – and multiply-selective – excitation without employing complex pulse envelope modulation[11].

It is also possible to directly perform three-dimensional NMR imaging by employing two simultaneous orthogonal phase encode gradients followed by frequency encode during signal readout. In this case, hard RF pulse/s are employed to generate and/or refocus transverse magnetization from the entire object. The amplitudes of the two phase encode gradients are incremented independently from experiment to experiment, eg. holding one fixed while the other is cycled through its full set of values, before incrementing the first and looping through the second, etc. Three-dimensional Fourier transformation then yields the desired three-dimensional image of the object. In general, 3D NMR imaging is clearly more time consuming than multi-slice 2D experiments, which are therefore preferred especially in the clinical context. A gradient echo 3D sequence is shown in Figure 9.

Projection reconstruction techniques – see for example the pulse sequence in Figure 10 – are especially valuable for investigations of materials that have short spin–spin relaxation times T_2; in such cases, the phase memory time could be shorter than the gradient switch-

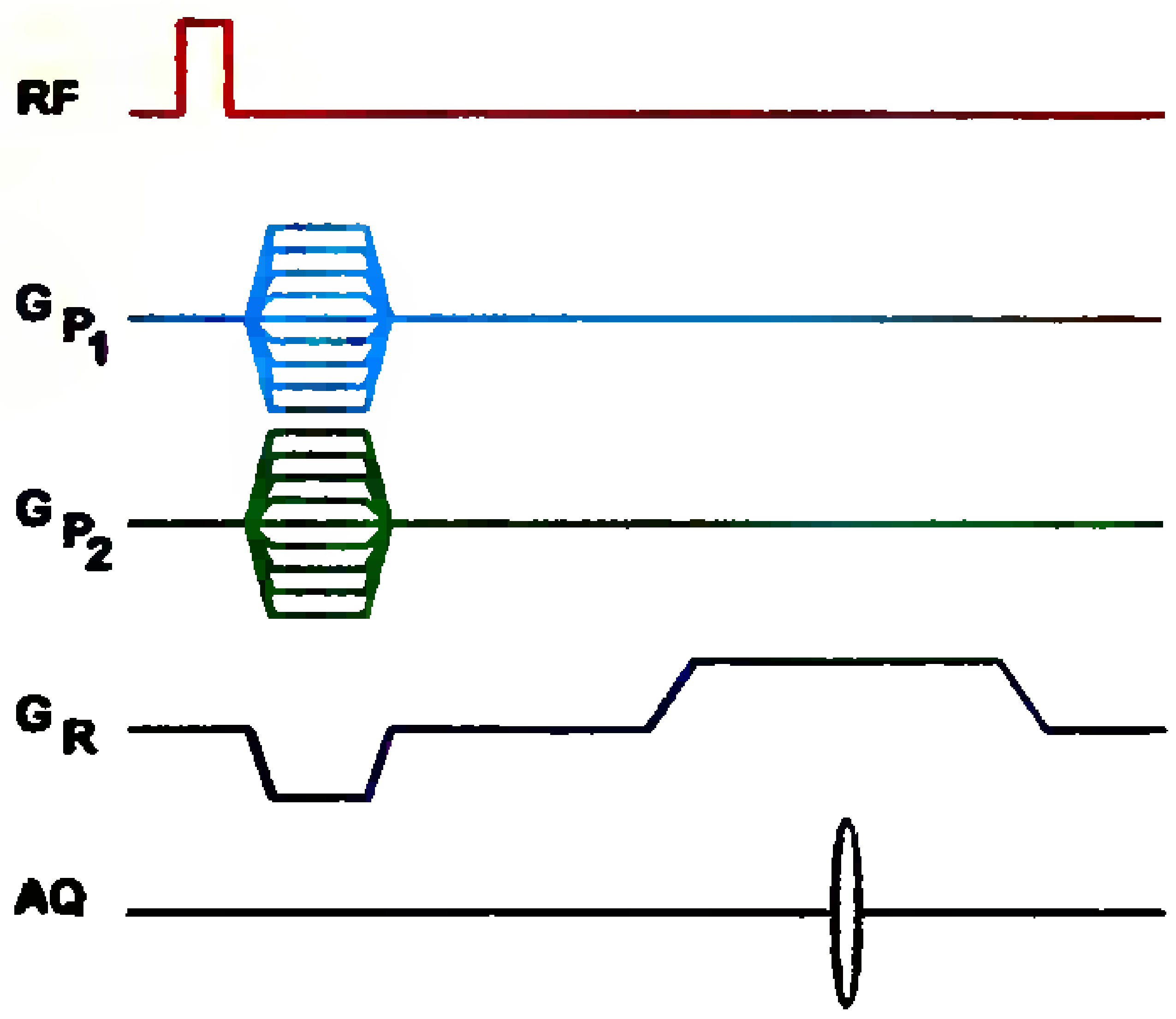

Figure 9. Gradient echo MR imaging sequence for three-dimensional imaging. Note here again that the two-phase encodes may be telescoped into one and the same evolution interval, with independent incrementation of the corresponding gradient amplitudes from experiment to experiment to generate the 3D dataset. Clearly, this mode minimizes the constant T_2 losses over the entire dataset. In 3D NMR spectroscopy, on the other hand, the two variable evolution times must normally follow one another.

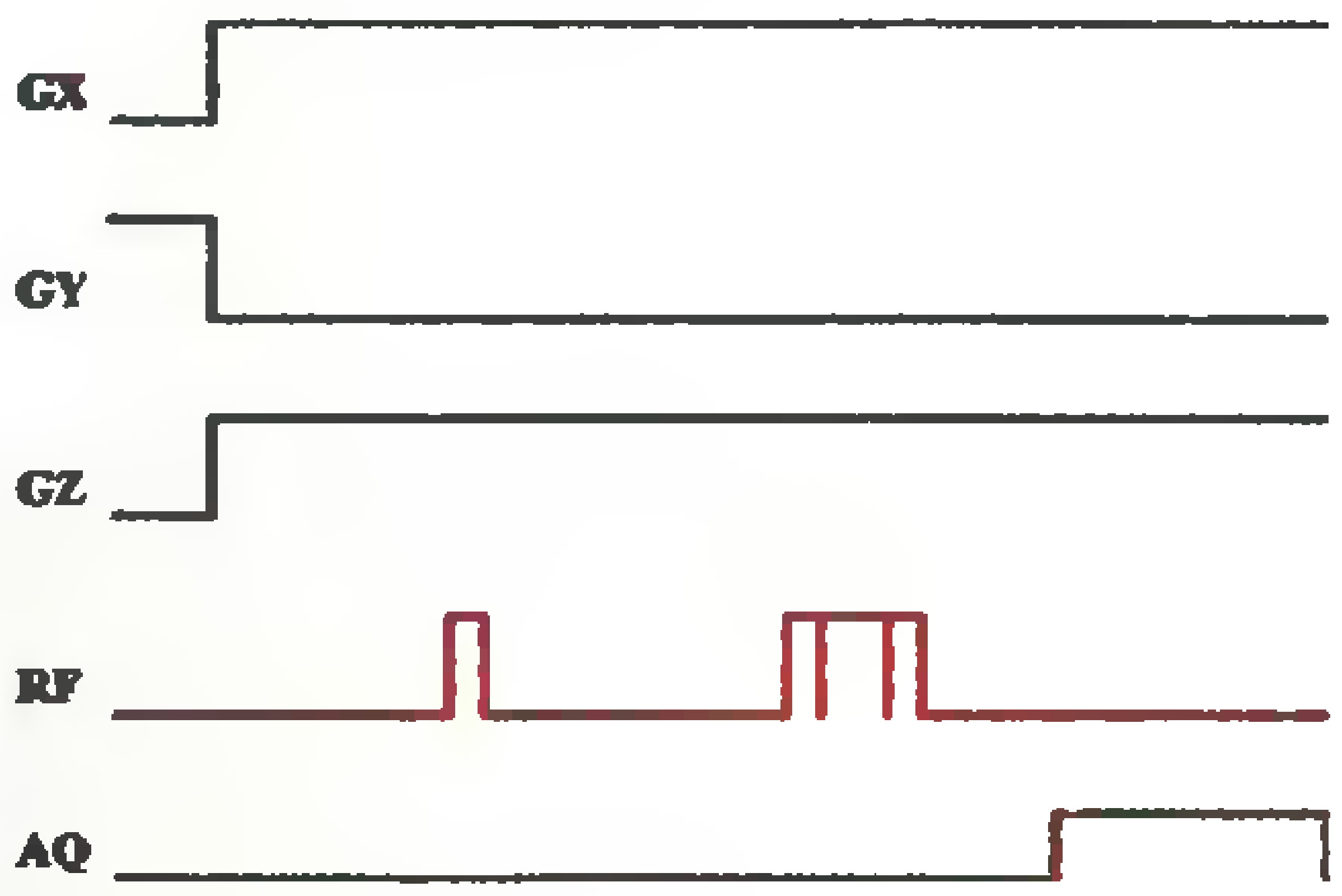

Figure 10. Spin echo pulse sequence for 3D projection reconstruction imaging.

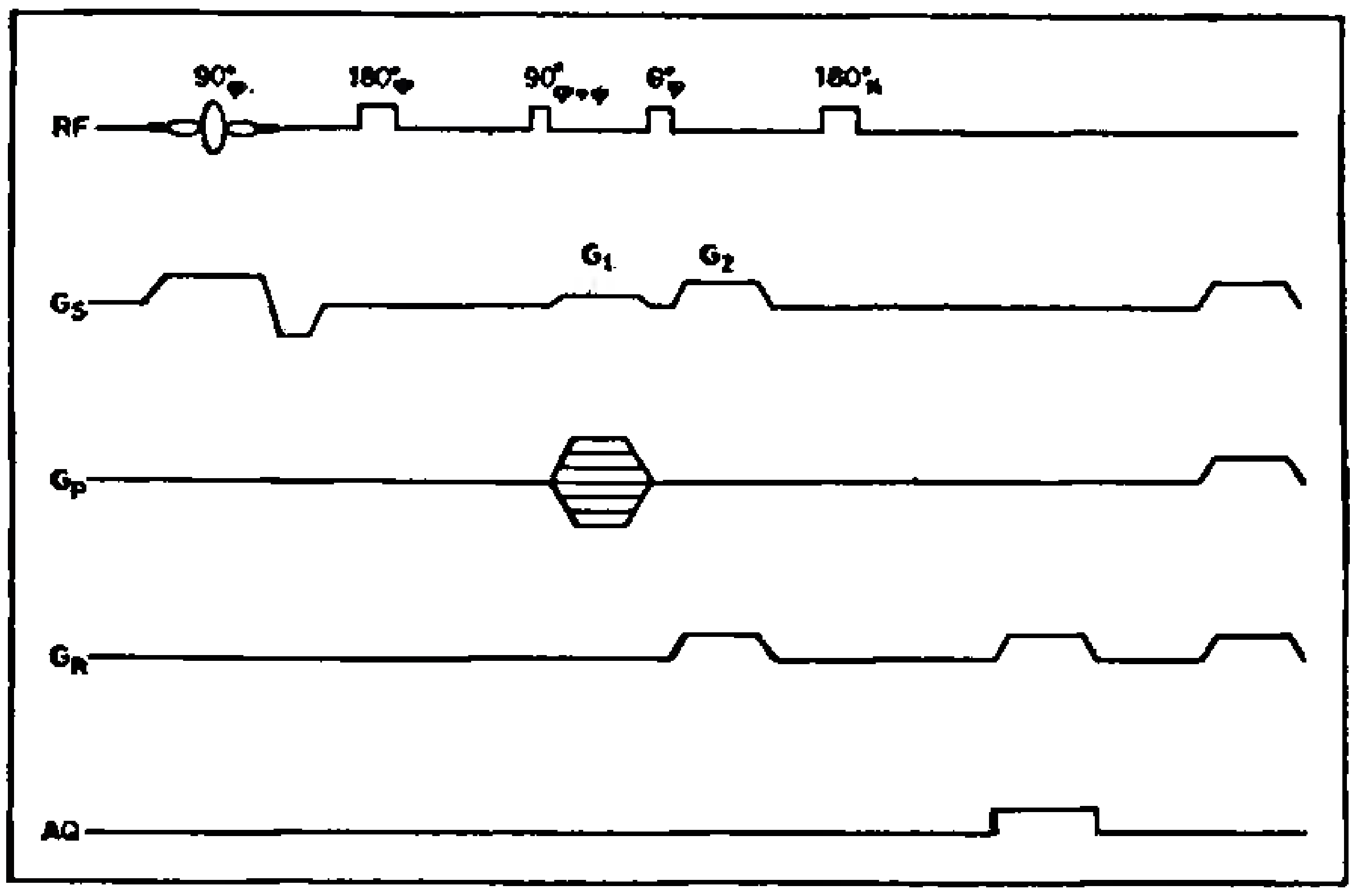

Figure 11. Pulse sequence for slice selective 2D *M*ultiple Q*U*antum–*S*ingle *Q*uantum (MUSQ) imaging.

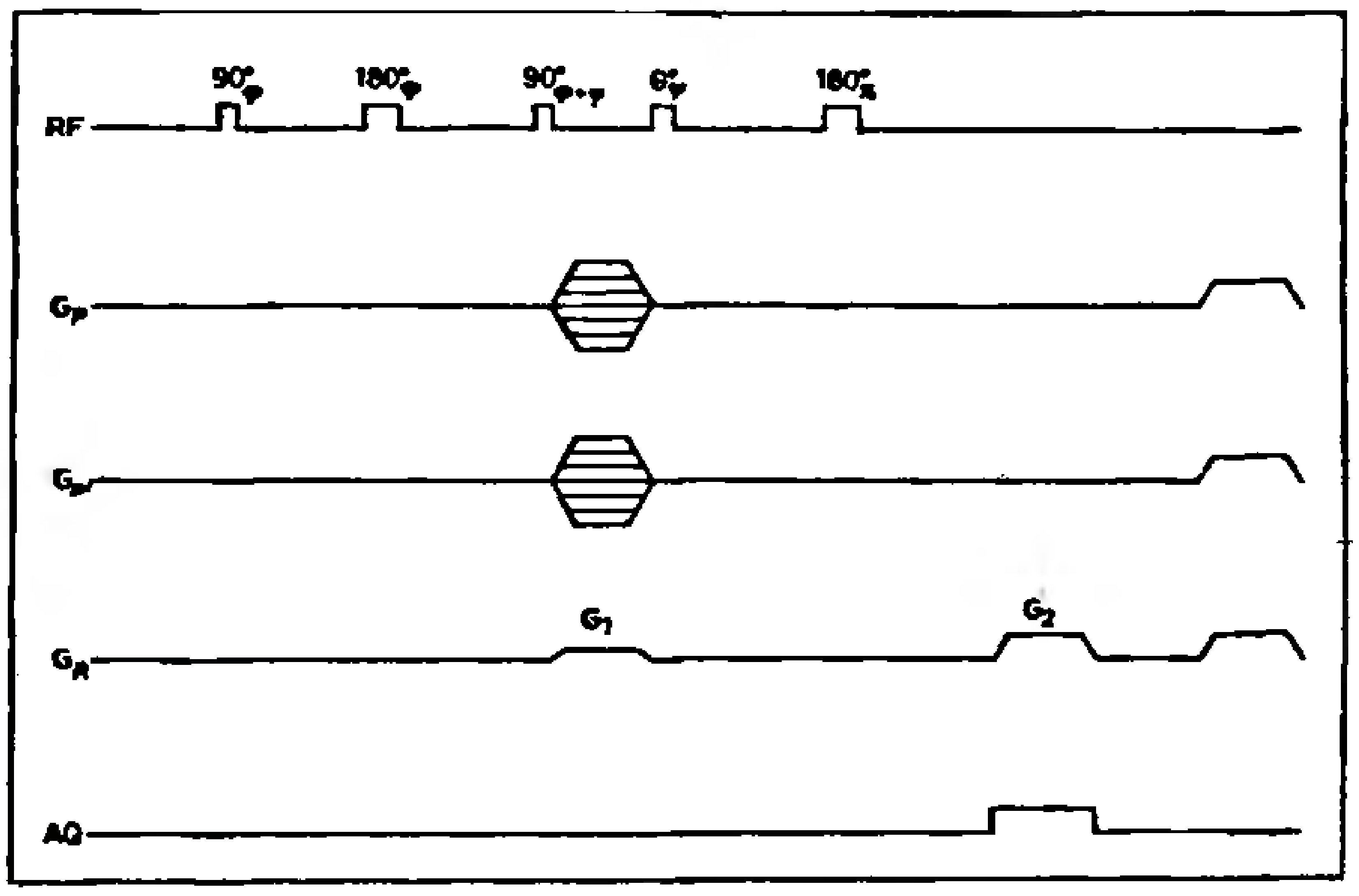

Figure 12. Pulse sequence for three-dimensional *M*ultiple Q*U*antum–M*U*ltiple Quantum–*S*/ngle *Q*uantum (MUUSIQ) imaging.

ing time, rendering the Fourier imaging concept unworkable. This situation demands that the gradients be switched on and stabilized before transverse magnetization is created, a 2D or 3D experiment then being carried out with systematic reorientation of the gradient in successive passes. Note that the type of **k** space raster involved here implies that the sample point density in the outer regions of **k** space is lower than that near the origin of **k** space: this would give rise to distortions in the image and in practice compels data interpolations. As against this, it is to be noted that the Fourier imaging protocol leads to a uniform density of sampling points in **k** space.

It is also possible to perform imaging of specific metabolites, suppressing the 110 M water proton signal *in vivo* and encoding the desired metabolite resonances. This has been achieved for example in brain imaging of normal volunteers as well as of astrocytoma patients[12]. In the latter case, the distribution of specific metabolites such as choline, *N*-acetyl aspartate and lactate directly indicate the state of health and progress of therapy.

To achieve superior suppression of the water proton signal and at the same time ensure molecule-specific imaging, we recently developed multiple quantum imaging methods in our laboratory[13]. Conventional imaging techniques encode transverse magnetization as seen above, corresponding to single quantum coherences (SQCs) in the spin system. Multiple Quantum Coherences (MQCs) may be generated in a molecule-specific manner independent of chemical shifts by using scalar *J* couplings as the handle and may be phase encoded. Note that *n*QCs effectively behave as spins with magnetogyric ratio $n\gamma$. Thus the expression (eq. 7) for the field-of-view in the phase encode direction/s is scaled down by a

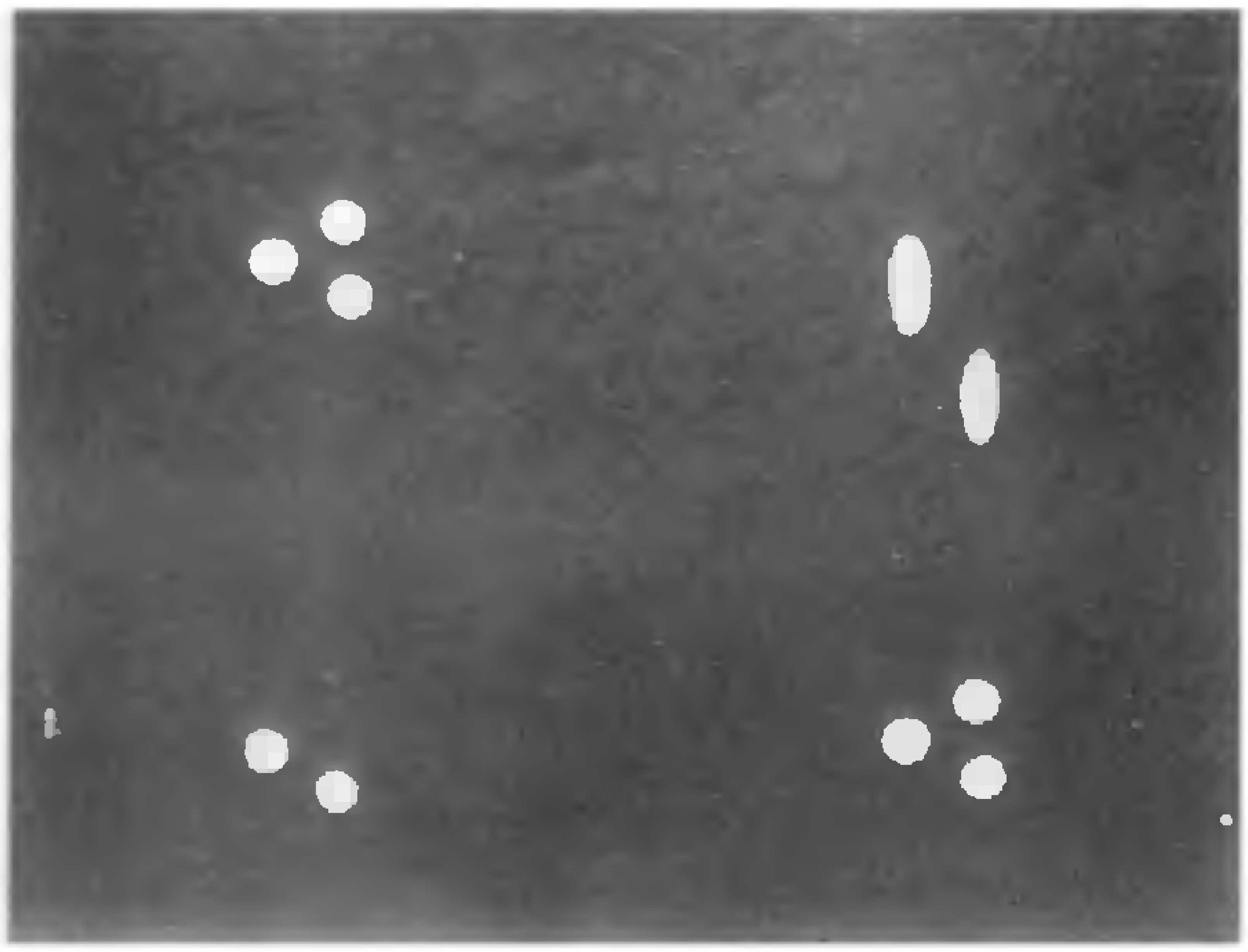

Figure 13. *Top left and bottom right*: Single-quantum slice-selected image of three-tube phantom (two tubes of ethanol and one of methanol). Sinc pulse for slice selection, slice thickness about 0.67 mm. The *xy* view perpendicular to the long axis (*z*) is shown. *Top right*: Triple-quantum-single-quantum MUSQ image of the phantom with normal phase-encode gradient. *Bottom left*: Triple-quantum-single-quantum MUSQ image of the phantom, with phase-encode gradient reduced by a factor of three. All images (128 × 128) were obtained on an 8.9 cm Bruker MSL300P system with an actively-shielded microimaging probehead, employing a 15 mm RF insert; gradient strengths about 7 G cm^{-1}.

Figure 14. *Top left and bottom right*: Single-quantum 3D image (*xy* view) of three-tube phantom similar to that in Figure 13. *Top right and bottom left*: Three-dimensional triple quantum MUUSIQ image (*xy* view) of the phantom, with normal phase-encode gradients, 64 (*x*) × 64(*y*) × 128 (*z*) images.

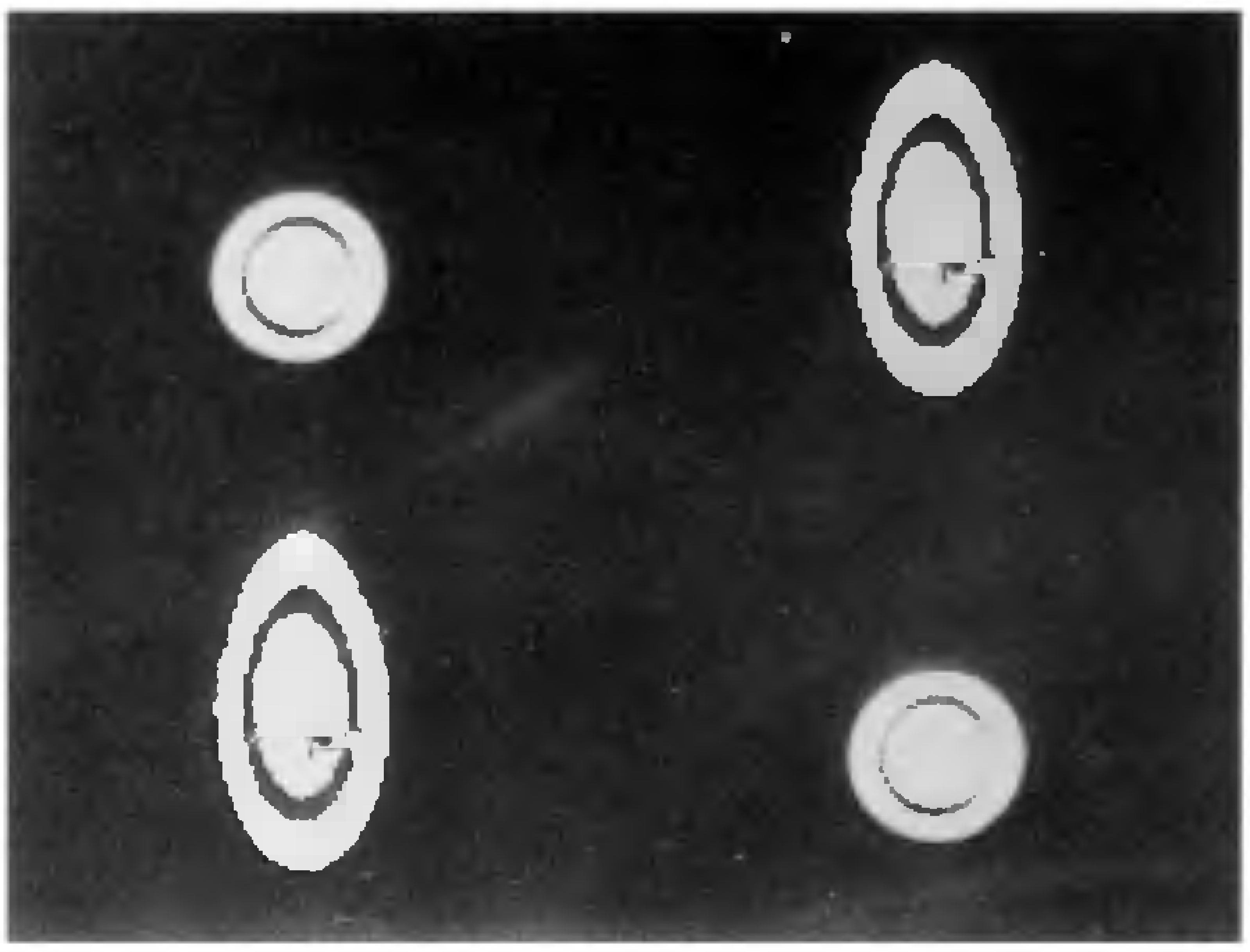

Figure 15. Single quantum spin echo image (displayed along the diagonal) and double quantum MUSQ image (displayed along the skew diagonal) of a two-tube phantom of ethanol.

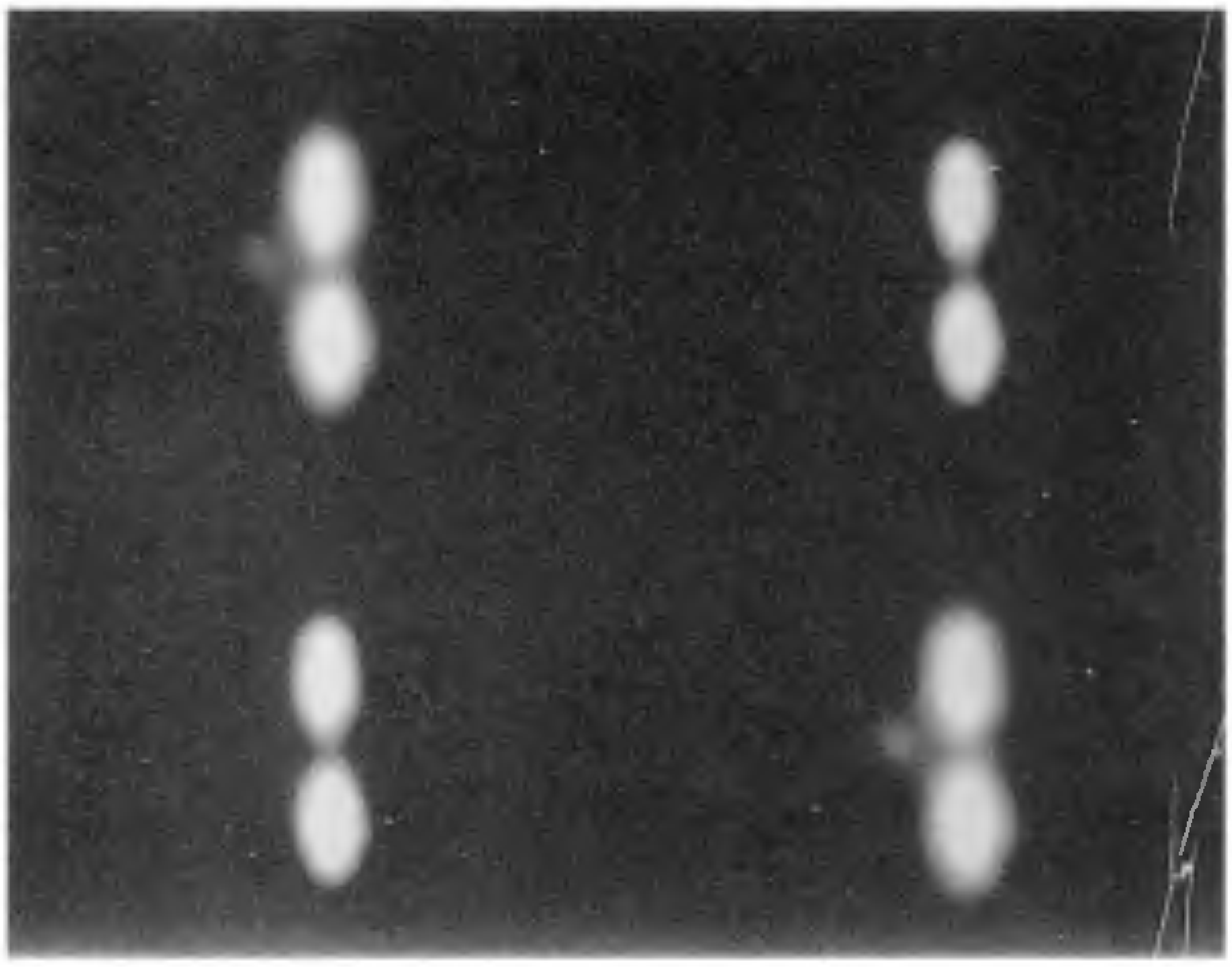

Figure 16. Double quantum MUSQ image of three-tube phantom: two tubes of a 60 mM aqueous solution of lactate and a third tube of water. The images on the diagonal and skew diagonal display the same information at different intensity thresholds.

factor of *n*, which is equivalent to increased image resolution per unit applied field gradient in the phase encode direction/s. Further, the reduced FOV is not associated with a penalty in terms of increased receiver bandwidth, since signal acquisition does not occur during the phase encode period. We developed imaging sequences (Figures 11 and 12) which combine multiple quantum phase encode/s with single quantum frequency encode, so that line scans are possible in **k** space and one is not restricted to point scans as one might fear, given that MQCs are not directly observable and need to be converted to SQCs to register a signal in the MR receiver. Examples of two- and three-dimensional MQ imaging are given in Figures 13 and 14. Note that MQ T_2 contrast now becomes available with this method.

Figures 15 and 16 exhibit two applications of MUSQ. Figure 15 exhibits the image of a two-tube phantom,

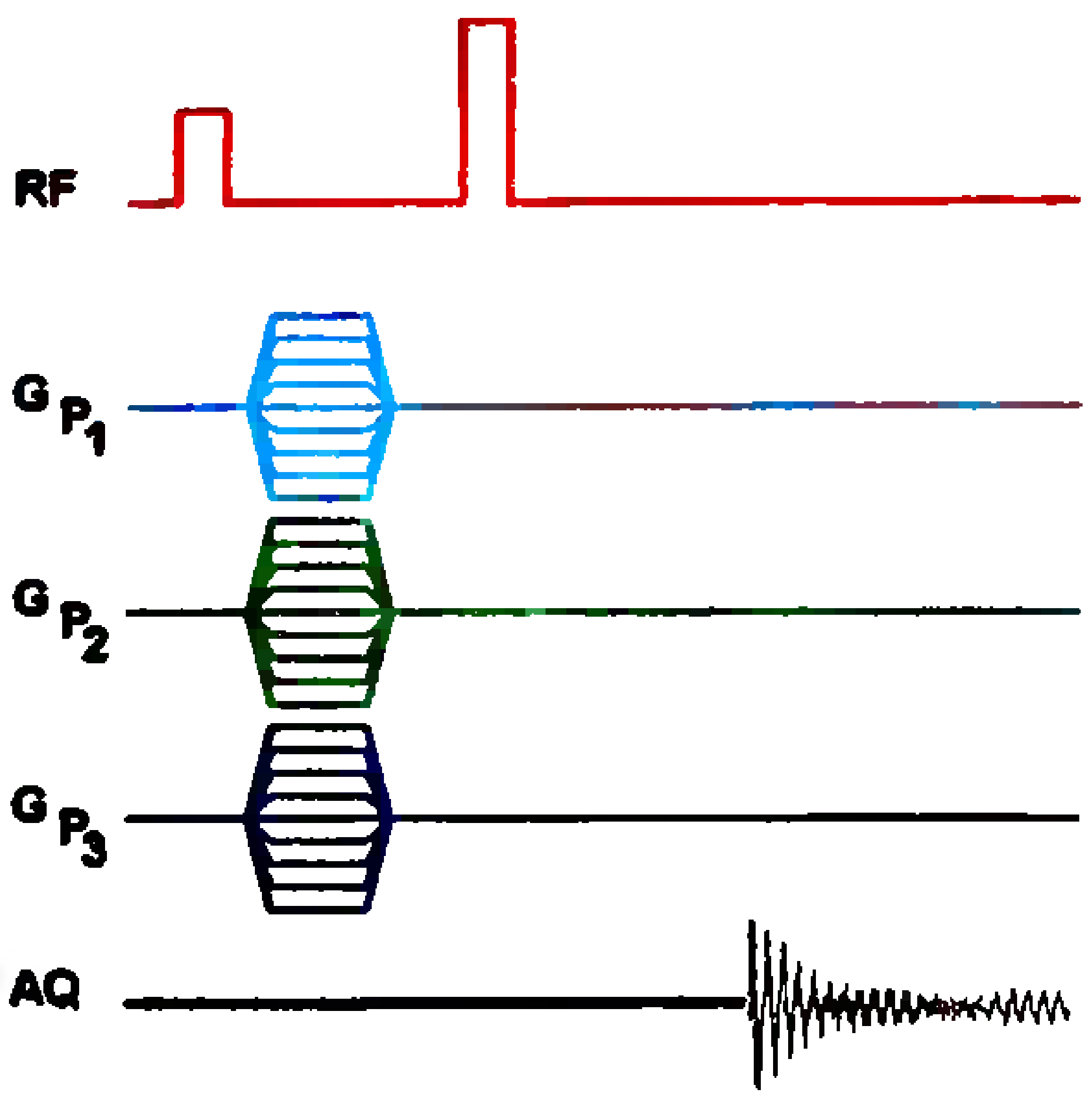

Figure 17. Pulse sequence for four-dimensional spatial-spectral imaging. Note that this mode has the advantage of data acquisition in the absence of a gradient, getting rid of the detection bandwidth penalty. Dephasing under shifts and offsets during the phase encode period is refocused by the hard π pulse. In reality, spatial-spectral information of metabolites *in vivo* can be obtained only if the sequence commences with water suppression; no magnetization transfer is involved in the course of this sequence.

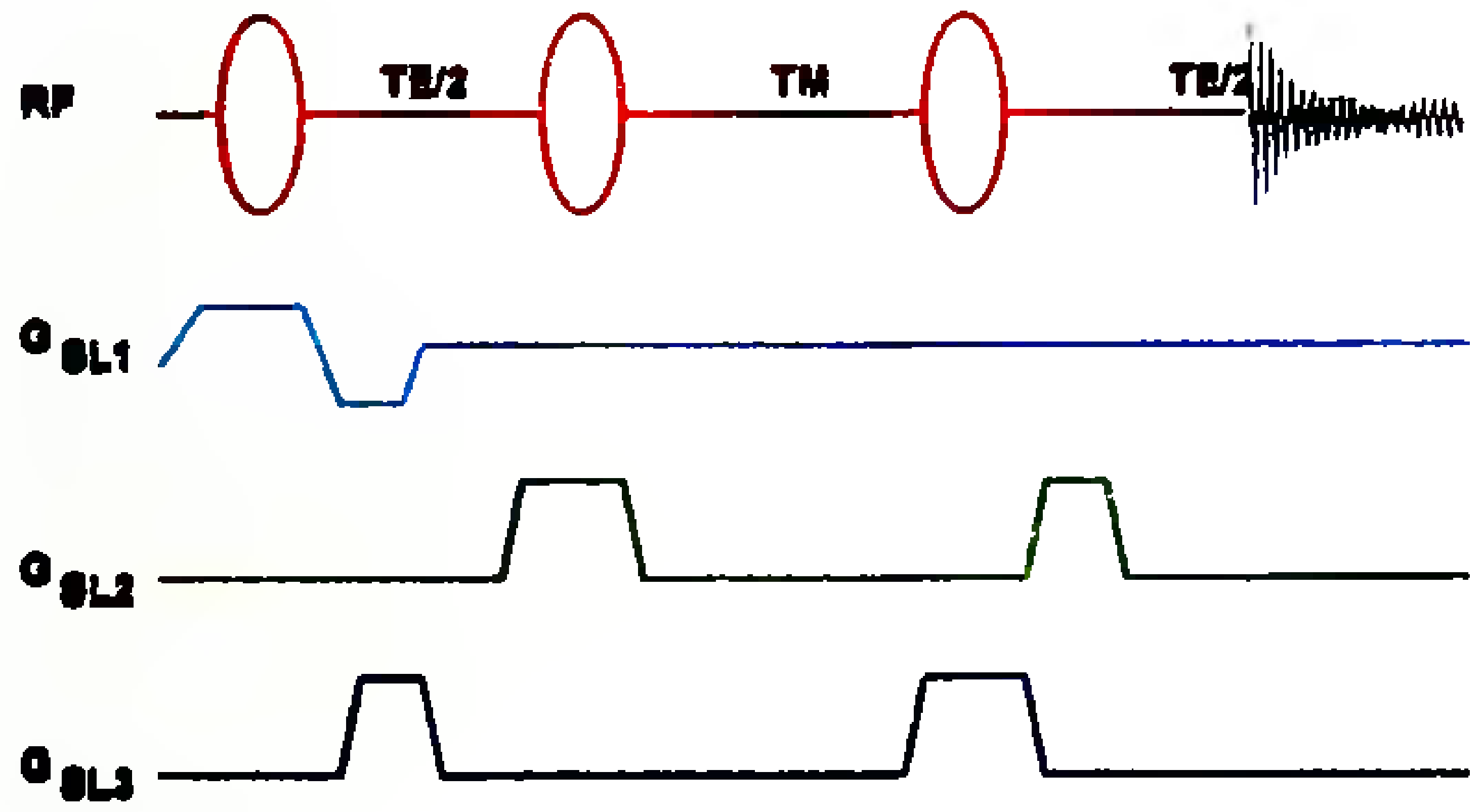

Figure 18. Pulse sequence for volume localized spectroscopy, i.e. spectroscopy of a single volume element in the sample. The stimulated echo signal is acquired.

both tubes containing ethanol. The normal spin echo image is displayed along the diagonal, while the double quantum MUSQ image is displayed along the skew diagonal. Note the magnification of the annular space in the MUSQ image of this phantom composed of two concentric tubes.

Figure 16 displays the image of a three-tube phantom, two tubes containing aqueous solutions of 60 mM lactate, while the third tube contains water. The double quantum MUSQ images are displayed along the skew diagonal, while the same are displayed along the diagonal at a lower intensity threshold, displaying the weak residual water signal from the third tube. Note the excellent water suppression.

Volume localized spectroscopy

It is possible to acquire – by means of the pulse sequence shown in Figure 17, for example – the high resolution spectrum of the entire object as a function of spatial co-ordinates of the 3D volume elements (voxels) into which the object is notionally divided.

This, however, is an inefficient spatial-spectral imaging experiment in the sense that three-dimensional **k** space is scanned point by point.

However, it is often of interest to obtain spectra not from all the voxels of an object simultaneously, but rather from a specific, well-defined volume element. One of the successful pulse sequences to achieve this is the STEAM (*ST*imulated *E*cho *A*cquisition *M*ode) sequence[14] shown in Figure 18.

The first pulse of the STEAM sequence selects a plane of spins, while the second orthogonal pulse produces longitudinal magnetization from the rod of intersection of the two planes; finally, the third orthogonal gradient recalls magnetization that is stored longitudinally from a single voxel that corresponds to the intersection of the plane defined by it with the rod previously selected. Note that the other dephasing gradients select the stimulated echo component of the signal to the exclusion of the FID components that result from each pulse and thus lead to single-scan voxel selection. This is to be contrasted against certain other multi-scan voxel selection protocols which rely on signal cancellation over the cycle of scans to select signal from the desired voxel.

The STEAM sequence has been employed with great success in collecting volume-localized spectra of both protons and phosphorus *in vivo*. Assignment of resonances to specific metabolites is, however, often a fairly tricky issue, given the fact that *in vivo* measurements are almost invariably carried out at low fields, ca. 2 *T*. We, therefore, developed volume localized 2D zero quantum spectroscopy[15] (ZQS) within the STEAM environment to help resolve such issues in *in vivo* applications. The chief modifications in adapting STEAM to *in vivo* 2D ZQS work consist in:

(i) optimization of preparation time for zero quantum coherence taking into account the severely damped *J* modulation that prepares the system for coherence transfer; note that *in vivo* proton linewidths are of the order of 5–7 Hz, which is in fact of the same order as homonuclear proton–proton couplings. This implies for instance that optimum creation of anti-phase magnetization for a coupling of 7 Hz occurs not for a TE/2 setting of ca. 70 ms, but rather for roughly half the value.

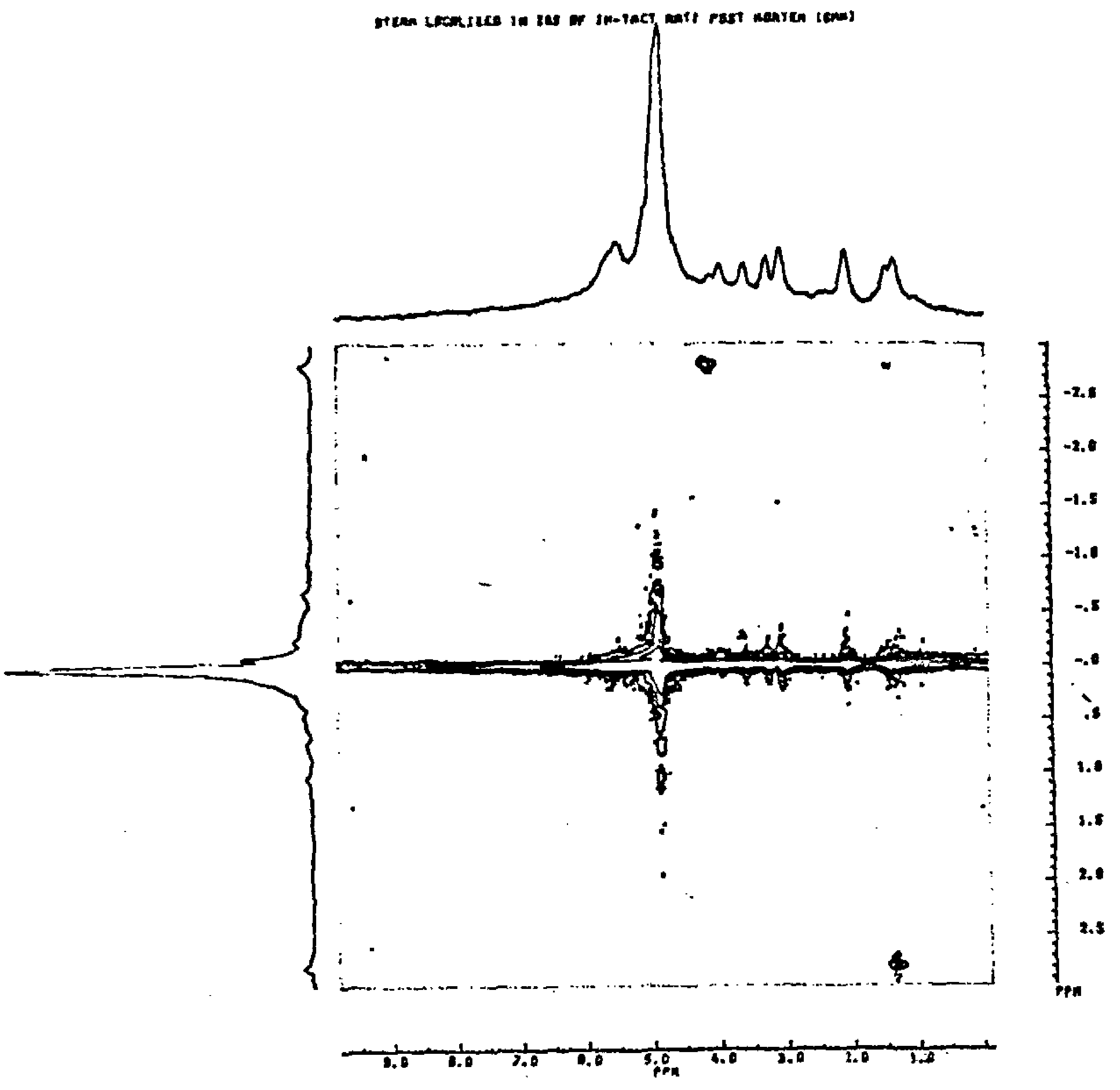

Figure 19. 2D volume localized zero quantum spectrum of rat brain post mortem, obtained on an intact, freshly killed rat. Voxel was a cube of side 6 mm. The measurements were performed on a 2.35 T system with 40 cm magnet equipped with an actively-shielded gradient assembly. (Chandrakumar, N., Gyngell, M. L., Helms, G. and Frahm, J., unpublished work.)

(ii) systematic variation of the TM value in the standard 2D fashion, but keeping a minimum value of a few ms.

(iii) reconversion pulse flip angle of 45° rather than 90°: this minimizes transfer of zero quantum coherence (ZQC) to passive spins. As a consequence, transfer of ZQC to the methine proton of lactate for instance, which otherwise occurs to an insignificant extent, is considerably enhanced. The methine proton resonates so close to the water protons as to normally go undetected. Also the *J*-echo signal is now collected to the exclusion of the normal stimulated echo signal.

Figure 19 displays the 2D volume localized zero quantum spectrum of a brain voxel of an intact rat, the experiment being carried out post mortem. Appearance of prominent lactate ZQ peaks in the spectrum is to be noted and especially the appearance of the peak at 4.12 ppm which unambiguously identifies the metabolite in question as lactate, and not threonine, for instance. We have also developed 1D spectral editing experiments in this environment.

NMR imaging of solids

In Figure 20 we give an example of a recent image from our laboratory[16] generated on a solid sample. Solid state NMR imaging is frought with peculiar problems that are not unlike the problems mentioned earlier in the context of ESR imaging. It has been recently realized that the large magnetic field gradients available at the fringe of a supercon magnet may be employed to generate the images of rigid solids[17]. The procedure here does not permit gradient re-orientation to generate a series of projections, since this would involve re-orientation of the magnet itself! Instead, the sample must be systematically re-oriented with respect to the magnet to generate the desired series of projections. The projections are then employed to reconstruct the desired image by

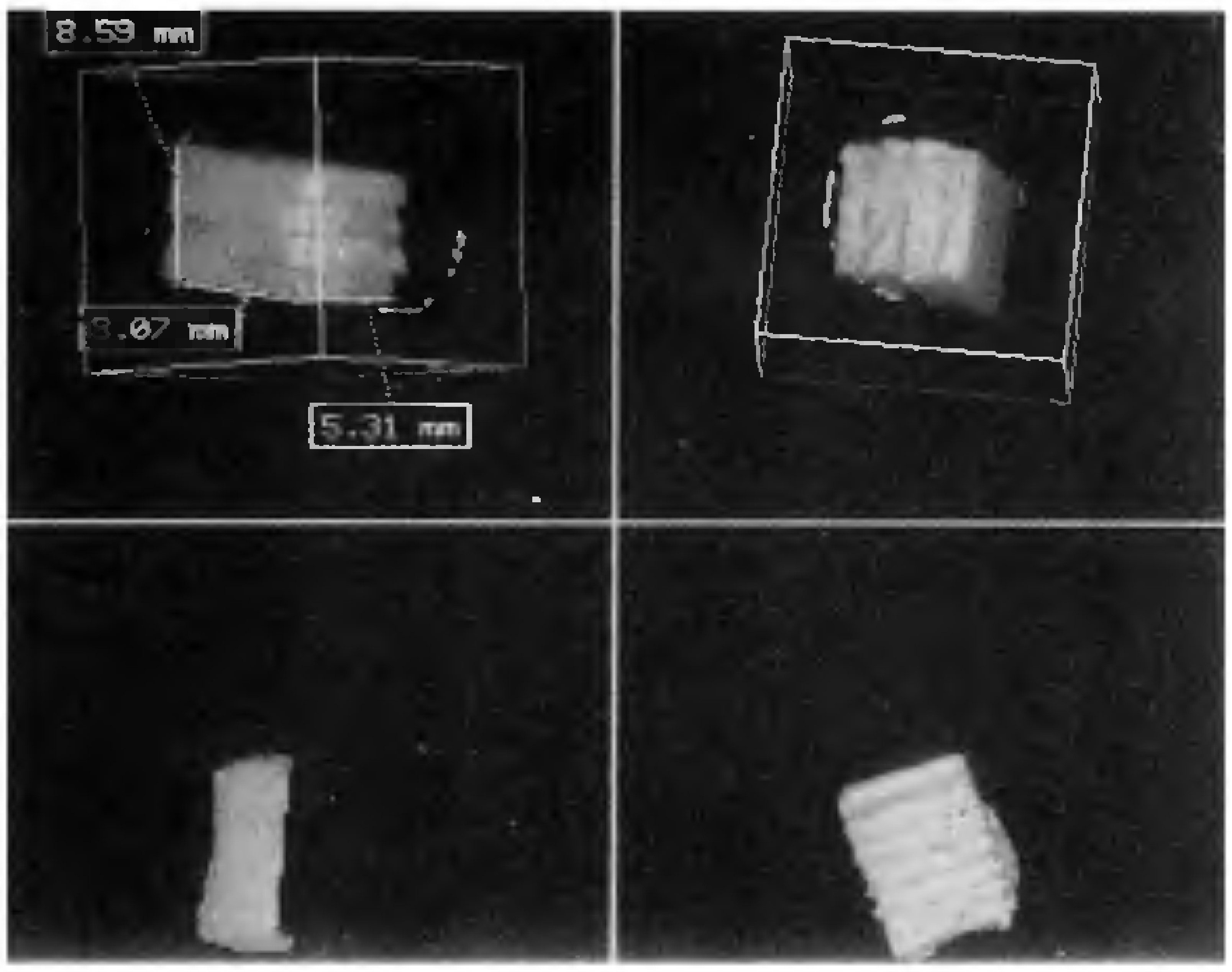

Figure 20. Various views of the STRAFI image of a phantom object composed of a stack of four mica-impregnated rubber sheets. *Top left*: surface reconstructed image from 3D STRAFI dataset (lateral view). *Top right*: Same as above, but frontal view. Note especially the cut-away section of one of the slices on the bottom right, clearly displaying dark stripes corresponding to the mica in the sheet.

means of standard back projection or filtered back projection techniques.

New prospects

In conclusion, it should also be mentioned that currently a quite different approach to NMR imaging is being pursued as well, which relies on force microscopy to detect MR, rather than the conventional coil-based inductive resonance detector. With extremely strong gradients induced by magnetic particles and an extremely sensitive cantilever system, micron level of image resolution has been achieved thus far by this method[18].

---

1. Lauterbur, P. C., *Nature*, 1973, **242**, 190.
2. Anil Kumar, Welti, D. and Ernst, R. R., *J. Magn. Reson.*, 1975, **18**, 69.
3. Morris, P. G., *NMR Imaging in Medicine and Biology*, Clarendon Press, Oxford, 1986.
4. Callaghan, P. T., *Principles of NMR Microscopy*, Clarendon Press, Oxford, 1991.
5. Ogawa, S., Lee, T. M., Kay, A. R. and Tank, D. W., *Proc. Natl. Acad. Sci. USA*, 1990, **87**, 9868.
6. Ljunggren, S., *J. Magn. Reson.*, 1983, **54**, 338.
7. Mansfield, P. and Maudsley, A. A., *J. Phys. C: Solid State Phys.*, 1976, **9**, L409.
8. Haase, A., Frahm, J., Matthaei, D., Hänicke, W. and Merboldt, K.-D., *J. Magn. Reson.*, 1986, **67**, 258.
9. Hennig, J., Nauerth, A. and Friedburg, H., *Magn. Reson. Med.*, 1986, **3**, 823.
10. Müller, S., *NMR: Basic Principles and Progress* (eds Diehl, P., Fluck, E., Günther, H., Kosfeld, P. and Seelig, J.), 1992, vol. 26, p. 171.
11. Chandrakumar, N., Patent Application No. NF-234/95, 1995.
12. Moonen, C. T. W., van Zijl, P. C. M., Frank, J. A., Le Bihan, D. and Becker, E. D., *Science*, 1990, **250**, 53.
13. Chandrakumar, N. and Sendhil Velan, S., *J. Magn. Reson.*, 1993, **A104**, 115.
14. Granot, J., *J. Magn. Reson.*, 1986, **70**, 488; Kimmich, R. and Hoepfel, D., *J. Magn. Reson.*, 1987, **72**, 379; Frahm, J., Merboldt, K.-D. and Hänicke, W., *J. Magn. Reson.*, 1987, **72**, 502.
15. Chandrakumar, N., Indo-USSR Symposium on Magnetic Resonance, 1991; National Workshop on Localized NMR, 1991.
16. Victor Babu, K., Setua, D., Rajagopalan, P. T. and Chandrakumar, N., NMRS, 1996.
17. Zick, K., *Nondestr. Test. Eval.*, 1994, **11**, 255.
18. Sidles, J. A., Garbini, J. L., Bruland, K. J., Rugar, D., Züger, O., Hoen, S. and Yannoni, C. S., *Rev. Mod. Phys.*, 1995, **67**, 249.

ACKNOWLEDGEMENTS. I acknowledge financial support for our NMR imaging research from CSIR and DRDO. Mr S. Sendhil Velan, Mr S. Venkata Raman and Mr K. Victor Babu have contributed to much of the original work from my laboratory described in this paper.